Monthly Notices
of the
ROYAL ASTRONOMICAL SOCIETY

MNRAS **445,** 3092–3104 (2014) doi:10.1093/mnras/stu1701

Modelling the ages and metallicities of early-type galaxies in Fundamental Plane space

L. A. Porter,[1,2★] R. S. Somerville,[3] J. R. Primack,[1,2] D. J. Croton,[4] M. D. Covington,[1,2†] G. J. Graves[5] and S. M. Faber[6]

[1]*Department of Physics, University of California, Santa Cruz, CA 95064, USA*
[2]*Santa Cruz Institute for Particle Physics, University of California, Santa Cruz, CA 95064, USA*
[3]*Department of Physics and Astronomy, Rutgers University, Piscataway, NJ 08854, USA*
[4]*Centre for Astrophysics and Supercomputing, Swinburne University of Technology, PO Box 218, Hawthorn, VIC 3122, Australia*
[5]*Department of Astrophysical Sciences, Peyton Hall, Princeton, NJ 08540, USA*
[6] *UCO/Lick Observatory, Department of Astronomy and Astrophysics, University of California, Santa Cruz, CA 95064, USA*

Accepted 2014 August 17. Received 2014 August 7; in original form 2014 March 5

ABSTRACT

Recent observations have probed the formation histories of nearby elliptical galaxies by tracking correlations between the stellar population parameters, age and metallicity, and the structural parameters that enter the Fundamental Plane, size R_e, and velocity dispersion σ. These studies have found intriguing correlations between these four parameters. In this work, we make use of a semi-analytic model, based on halo merger trees extracted from the Bolshoi cosmological simulation, that predicts the structural properties of spheroid-dominated galaxies based on an analytic model that has been tested and calibrated against an extensive suite of hydrodynamic+N-body binary merger simulations. We predict the R_e, σ, luminosity, age, and metallicity of spheroid-dominated galaxies, enabling us to compare directly to observations. Our model predicts a strong correlation between age and σ for early-type galaxies, and no significant correlation between age and radius, in agreement with observations. In addition, we predict a strong correlation between metallicity and σ, and a weak correlation between metallicity and R_e, in qualitative agreement with observations. We find that the correlations with σ arise as a result of the strong link between σ and the galaxy's assembly time. Minor mergers produce a large change in radius while leaving σ nearly the same, which explains the weaker trends with radius.

Key words: galaxies: elliptical and lenticular, cD – galaxies: evolution – galaxies: formation – galaxies: interactions.

1 INTRODUCTION

Nearby galaxies are commonly divided into two basic morphological types: spheroid-dominated, 'early-type' galaxies, and disc-dominated, 'late-type' galaxies. Early-type galaxies are dominated by random motions, have compact, concentrated light profiles, and are typically red and gas poor, while late-type galaxies are rotation supported, have more extended light profiles, and tend to be gas-rich, blue, and star forming.

Early-type galaxies lie on a two-dimensional plane relating effective radius (R_e), central stellar velocity dispersion (σ), and effective surface brightness (I_e), termed the Fundamental Plane (FP; Djorgovski & Davis 1987; Dressler et al. 1987; Faber et al. 1987). This plane is tilted from the plane one would expect from a simple application of the virial theorem, indicating that further processes, such as non-homology (i.e. differences in the density profile and orbital distribution) or a varying mass-to-light ratio, must have an effect (Jørgensen, Franx & Kjaergaard 1996). Furthermore, the FP is not an exact relation; galaxies have a degree of scatter around the FP, in effect making the FP 'thick'. Observations indicate that this scatter increases with redshift, particularly among less massive galaxies (Treu et al. 2005b).

More specifically, while the slope of the FP appears unchanged for high-mass ellipticals since $z \sim 1$, low-mass ellipticals at high

★ E-mail: lauren.porter@gmail.com
† NSF International Research Fellow, Karst Research Institute ZRC SAZU, Titov trg 2, SI-6230 Postojna, Slovenia.

redshifts have higher surface brightnesses than their effective radii and velocity dispersions would seem to predict (van der Wel et al. 2004; Treu et al. 2005a,b; Jørgensen et al. 2006; van Dokkum & van der Marel 2007). If we consider a projected FP, where surface brightness is the dependent parameter, then these low-mass galaxies tend to lie above the mean FP relation at high redshift (i.e. they are brighter than average), and to fall on to the FP over time.

There are indications that this residual thickness in the FP correlates with the stellar population age. Forbes, Ponman & Brown (1998) and Terlevich & Forbes (2002) found that galaxies with higher residual surface brightnesses are younger than those that lie near the mid-plane of the FP; conversely, those with lower residual surface brightnesses are older.

Recently, observations from the Sloan Digital Sky Survey (SDSS) have been used to analyse stellar population trends both within the* R–σ projection of the FP, and through the thickness of the FP, using residual surface brightnesses (Graves, Faber & Schiavon 2009a,b, 2010; Graves & Faber 2010). By stacking spectra of galaxies with similar stellar properties and measuring the Lick indices on those spectra, the authors were able to derive [Fe/H], [Mg/H], [Mg/Fe], and stellar age for a population of passive early-type galaxies. In agreement with Forbes et al. (1998) and Terlevich & Forbes (2002), Graves et al. (2009b, hereafter G09) found that younger galaxies lie above the FP, and have relatively higher surface brightnesses, while older galaxies lie below it. Galaxies above the FP also tended to have higher [Fe/H] and [Mg/H], and lower [Mg/Fe]. G09 also determined that age, [Fe/H], [Mg/H], and [Mg/Fe] increase with velocity dispersion throughout the FP, independent of the residual surface brightness. These same properties are almost independent of R_e, indicating that a galaxy's velocity dispersion, and not its dynamical mass ($\propto \sigma^2 R_e$), has the better correlation with its star formation history. The strong dependence of age and metallicity on velocity dispersion is consistent with previous studies (Nelan et al. 2005; Smith, Lucey & Hudson 2007) and more recent studies (Thomas et al. 2010; Greene et al. 2012; Johansson, Naab & Ostriker 2012). Similar results were obtained in a recent analysis of the Six-degree Field Galaxy Survey (6dFGS; Jones et al. 2004, 2009) by Springob et al. (2012), though this work finds a slightly stronger dependence of age and metallicity on effective radius.

The physical origin of the FP, its slope and evolution, and correlations between the structural parameters that enter it and stellar population parameters such as age and metallicity remain somewhat poorly understood. A wide variety of mechanisms have been proposed to explain the formation of spheroids and the apparent transformation of gas-rich, star-forming, disc-dominated galaxies into gas-poor, passive spheroid-dominated galaxies that seems to be implied by observations of high-redshift galaxies (Bell et al. 2007; Faber et al. 2007). Based on an early generation of numerical simulations, a 'merger' picture was proposed in which elliptical galaxies are formed through 'major' (near equal-mass) mergers of disc galaxies (e.g. Toomre & Toomre 1972; Toomre 1977; Mihos & Hernquist 1994; Barnes & Hernquist 1996). More recently, it has been realized that the picture is more probably more complex: the chemical, dynamical, and structural properties of local giant ellipticals are not consistent with having been formed through a single binary merger between progenitors similar to nearby large spirals like the Milky Way. Rather, mergers at high redshift probably involve progenitors that are denser and more gas rich than our Galaxy, leading to more compact remnants (Khochfar & Burkert 2003; Dekel & Cox 2006; Ciotti, Lanzoni & Volonteri 2007; Wuyts et al. 2010). Subsequent dissipationless 'dry' mergers and minor mergers can greatly increase the galaxies' stellar masses and radii (Naab, Khochfar & Burkert 2006; Bezanson et al. 2009; Naab, Johansson & Ostriker 2009; Oser et al. 2012; Hilz, Naab & Ostriker 2013; Laporte et al. 2013). Thus the massive ellipticals seen in the local universe are probably built up through a complex sequence of multiple mergers, including 'wet' (gas-rich), moist and dry mergers, major and minor mergers, and mergers between progenitors with a variety of morphologies and sizes (Khochfar & Silk 2006).

However, mergers may not be the only possible way to create a spheroid-dominated galaxy. It has been proposed that spheroids may also form through *in situ* processes associated with gravitational instabilities, such as via the formation of a bar that destabilizes the disc, transferring mass into a spheroid component (Toomre 1964; Hohl 1971; Ostriker & Peebles 1973; Combes et al. 1990; Debattista et al. 2004) and via clumps of gas that form in the disc and migrate inwards (Dekel et al. 2009, 2013; Bournaud et al. 2011). Some studies based on semi-analytic models suggest that formation of spheroids through a non-merger channel is necessary in order to account for the observed fraction of spheroid-dominated galaxies at intermediate masses (Parry, Eke & Frenk 2009; De Lucia et al. 2011; Porter et al. 2014). However, the efficiency of spheroid formation via disc instabilities, its physical basis, and its importance relative to mergers remain poorly understood issues.

Currently available numerical hydrodynamic simulations of cosmological volumes typically do not have adequate resolution to robustly resolve the internal structure of galaxies. Moreover, it is well known that the observed properties of early-type galaxies cannot be reproduced without introducing a process that quenches star formation and prevents overcooling in massive objects, such as feedback from active galactic nuclei (AGN). Implementing black hole growth and AGN feedback in a physical manner requires even higher resolution. Therefore, although much recent progress has been made, making accurate predictions of galaxy internal structure for statistically robust samples remains challenging for numerical simulations.

Semi-analytic models (SAMs) provide an alternative method to simulate the formation and evolution of galaxies in a cosmological context. SAMs are also unable to resolve the internal structure of galaxies. The advantage instead is that alternative prescriptions for physical processes can be more efficiently implemented into SAMs, and a larger sample of model galaxies can be studied. Recent SAMs that include schematic recipes for AGN feedback have proven to be quite successful in reproducing a variety of observed global galaxy properties (e.g. Bower et al. 2006; Croton et al. 2006; Somerville et al. 2008, 2012; Fontanot et al. 2009; Guo et al. 2011). In Porter et al. (2014, hereafter P14), we incorporated a model for predicting the sizes and velocity dispersions of spheroids formed in mergers and disc instabilities within the 'Santa Cruz' SAM of Somerville et al. (2008, 2012, hereafter S08, S12, respectively). In this new generation of models, the SAM is implemented within merger trees extracted from the Bolshoi cosmological N-body simulation (Klypin, Trujillo-Gomez & Primack 2011; Trujillo-Gomez et al. 2011) using the ROCKSTAR halo finder and the gravitationally consistent merger tree algorithm developed by Behroozi et al. (2013). The model for the structural properties of merger remnants is motivated and calibrated based on high-resolution numerical smoothed particle hydrodynamic simulations of binary galaxy mergers (Cox 2004; Cox et al. 2006, 2008; Johansson, Naab & Burkert 2009). An earlier version of this model was presented in Covington et al. (2008, hereafter C08), and applied in post-processing to mergers extracted from SAMs in Covington et al. (2011, hereafter C11).

In P14, we extended the model of C08 to treat mergers between progenitors spanning a wider variety of gas fractions and

morphology, including gas-poor and spheroid-dominated galaxies, using the simulation suite of Johansson et al. (2009). P14 implemented this more general model for the structural properties of merger remnants, along with a simple model for estimating the structural properties of spheroids formed via disc instabilities, self-consistently within the Santa Cruz SAM, and showed that the new SAM reproduces the observed stellar mass function and FP scaling relations of spheroid-dominated galaxies in the local universe. In addition, the model qualitatively reproduces the observed evolution of the size–mass relation for spheroid-dominated galaxies from $z \sim 2$–0, and the steeper slope, smaller scatter, and more rapid evolution of the size–mass relation for spheroid-dominated relative to disc-dominated galaxies. The model also predicts weaker evolution in the Faber–Jackson (mass–velocity dispersion) relation than in the size–mass relation, in agreement with observations.

A key aspect of our model for spheroid structure is the accounting for dissipation during mergers of progenitors that contain significant amounts of gas. Unlike stars, gas can radiate energy away, and therefore mergers between gas-rich progenitors result in more compact remnants (C08; Hopkins & Beacom 2008). Previous SAMs that attempted to model spheroid sizes without accounting for this dissipation were not able to reproduce observed structural scaling relations (Cole et al. 2000; Guo et al. 2011; Shankar et al. 2013).

In this paper, we use the model developed by P14 to make predictions for the relationship between early-type galaxies' *structural parameters* (radius and velocity dispersion) and their *stellar population parameters* (age and metallicity). We select spheroid-dominated galaxies from our models and determine their location within the FP using the same approach as that of the observational study of G09, to which we compare our predictions explicitly. We then examine the predicted correlations between galaxies' age and metallicity as a function of velocity dispersion and radius, for slices taken below, within, and above the FP. In this way, we hope to better understand the origin of the observed correlations.

Section 2.1 briefly describes the SAM used in our analysis. Section 2.2 provides a brief overview of the analytic model used to calculate the radius and velocity dispersion for spheroids. Section 3 presents a summary of the observations of G09, to which we make direct comparisons. We present results beginning in Section 4, in which we examine the relationships between either age or metallicity as a function of velocity dispersion and radius, for different slices of the early-type population from the P14 SAM taken parallel to the FP as described above. We discuss the interpretation of our results in Section 5.

2 METHODS

We provide a very brief overview of the SAM used in this work. For more details, see S08, S12, and P14. We also give a brief summary of our prescription for computing the effective radii and velocity dispersions of spheroids, as developed in C08, C11, and P14.

2.1 The semi-analytic model

The P14 SAM is implemented within merger trees extracted from the Bolshoi *N*-body dark matter (DM) simulation (Klypin et al. 2011; Trujillo-Gomez et al. 2011) using the ROCKSTAR algorithm and the gravitationally consistent merger trees by Behroozi et al. (2013). We follow the merging and tidal destruction of satellites within virialized haloes using a SAM described in S08. To predict the observable properties of galaxies, we adopt fairly standard prescriptions for photoionization, radiative cooling, star formation, supernova feedback, chemical evolution, and black hole growth and feedback (see S08 and P14 for details). We model the spectral energy distribution of galaxies by convolving our predicted star formation and chemical enrichment histories with the stellar population synthesis models of Bruzual & Charlot (2003). We include dust extinction using analytic prescriptions as described in S12.

We adopt the same cosmological parameters used in the Bolshoi simulation: $\Omega_{\rm m} = 0.27$, $\Omega_\Lambda = 0.73$, $h = 0.70$, $\sigma_8 = 0.82$. These are consistent with the *Wilkinson Microwave Anisotropy Probe* five- and seven-year results (Komatsu et al. 2009, 2011). Throughout this work, we adopt a Chabrier (Chabrier 2003) stellar initial mass function (IMF).

2.2 Model for spheroid structural parameters

To compute the structural properties of galactic spheroids, we have built upon the model developed by C08 and C11. We first consider spheroids that are formed in mergers. In the case of a merger without dissipation, simple conservation of energy arguments would predict that the internal energy of the two progenitors is conserved during the merger:

$$E_{\rm init} = E_{\rm f} = C_{\rm int} \sum_{i=1}^{2} G \frac{(M_{*,i} + M_{{\rm new}*,{\rm i}})^2}{R_{*,i}} = C_{\rm int} G \frac{M_{*,{\rm f}}^2}{R_{*,{\rm f}}}, \quad (1)$$

where $M_{*,i}$ is the stellar mass of each of the two progenitors, $R_{*,i}$ are the three-dimensional effective radii of the progenitors, $M_{*,{\rm f}}$ and $R_{*,{\rm f}}$ are the stellar mass and 3D effective radius of the merger remnant, and $C_{\rm int}$ is a dimensionless constant relating the internal energy of the galaxy to GM^2/R.

As described in P14, the mass of new stars formed in the merger is computed using a fitting function based on the results of numerical binary merger simulations as described in Hopkins et al. (2009b) and implemented in Hopkins et al. (2009a) and S12. The fitting function depends on progenitor gas fraction and merger mass ratio.

However, in the presence of gas, mergers can be highly dissipative; thus the conservation of energy relation must be modified with a term incorporating radiative losses. Motivated by the results of hydrodynamical simulations, C08 provided a simple parametrization of this radiative energy loss:

$$E_{\rm rad} = C_{\rm rad} \sum_{i=1}^{2} K_i f_{{\rm g},i} f_{{\rm k},i} (1 + f_{{\rm k},i}), \quad (2)$$

where $K_i, f_{{\rm g},\,i}$, and $f_{{\rm k},\,i}$ are the total kinetic energy, baryonic gas fraction, and fractional impulse of progenitor i, $C_{\rm rad}$ is a dimensionless constant and the sum is over the two progenitors. The energy equation above must be modified by including this term: $E_{\rm init} + E_{\rm rad} = E_{\rm f}$. We use this equation to solve for the effective radius of the stars in the remnant, $R_{*,{\rm f}}$. For more details, please see appendix A in C08.

The model presented in C08 and C11 was limited in that it was only calibrated against simulations of fairly gas-rich mergers of disc-dominated progenitors. In P14, we extended the model by calibrating it with an additional 68 hydrodynamical simulations of binary mergers, described in Johansson et al. (2009), including both major and minor mergers of mixed-morphology and spheroid–spheroid mergers (i.e. mergers in which one or both progenitors contain a significant spheroidal component). Importantly, we found that the parameters $C_{\rm int}$ and $C_{\rm rad}$ differ significantly depending on the mass ratio of the merger and the morphology and gas content of the progenitors. A complete table of values for these parameters, measured from the binary merger simulations, is given in P14.

The value of $f_{\rm rad} \equiv C_{\rm rad}/C_{\rm int}$ can be thought of as characterizing the relative importance of dissipation; high values indicate more dissipation. We find that this value is highest for major mergers of two disc-dominated galaxies ($f_{\rm rad} = 5.0$), is lower for minor mergers between two disc-dominated galaxies ($f_{\rm rad} = 2.7$) and is zero for mergers where one or both of the galaxies is spheroid dominated. This latter subset of mergers is thus essentially dissipationless.

We use the virial theorem to determine the line-of-sight velocity dispersion of the spheroid:

$$\sigma^2 = \left(\frac{C_\sigma G}{2R_{\rm f}} \frac{M_{*,{\rm f}}}{(1 - f_{\rm dm,f})} \right), \quad (3)$$

where $M_{*,{\rm f}}$ is the stellar mass of the spheroid, $R_{\rm f}$ is the stellar half-mass radius of the spheroid, and C_σ is a dimensionless constant that accounts for the conversion between the three-dimensional effective radius and the line-of-sight projection of the velocity dispersion. We define $M_{\rm dm}$ to be the mass of DM within $R_{\rm f}$, and $f_{\rm dm,\,f} = M_{\rm dm}/(0.5M_{*,{\rm f}} + M_{\rm dm})$ to be the central dark matter fraction (DMF) of the remnant. (The factor of 0.5 multiplies $M_{*,{\rm f}}$ because $R_{\rm f}$ is the stellar half-mass radius.) In computing $M_{\rm dm}$, we assume that the DM halo density profile has a Navarro–Frenk–White functional form (Navarro, Frenk & White 1996) and use the halo concentration value recorded in the ROCKSTAR halo catalogue. The value of C_σ is again measured from the binary merger simulations and is found to be nearly the same in all cases (see P14).

In P14, we found that when we accounted for spheroid growth through mergers alone, our model did not produce enough intermediate mass spheroid-dominated galaxies in the local universe. We therefore considered models in which spheroids could form and grow via disc instabilities. When a disc is deemed unstable according to a Toomre-like criterion (Toomre 1964; Efstathiou, Lake & Negroponte 1982), we transfer stars or stars and cold gas from the disc to the spheroid component until the disc becomes marginally stable again. Following the prescription of Guo et al. (2011), we assumed that the stellar mass transferred forms a spheroid with half-mass radius equivalent to that of the unstable disc material, which then merges dissipationally with any existing spheroid (i.e. $C_{\rm rad} = 0$). We presented two models of disc instability, one in which only the stellar disc participates in the instability, and one in which both the stars and gas in the disc participate. These two models were tuned separately to reproduce the early-type stellar mass function. In this paper, we use the 'Stars+Gas DI' model described in P14. We showed in P14 that the 'Stars DI' model produces very similar results.

We note that we do not include environmental processes that could lead to morphological transformation, such as galaxy harassment, or tidal or ram pressure stripping. However, these processes are expected to be most important in galaxy clusters and should be subdominant in field galaxy samples, on which we focus here. Some readers might be concerned that neglecting stripping processes could affect the cold gas fractions of satellites, which would impact the degree of dissipation experienced in a merger. However, tidal stripping should not change the gas *fraction*, and strong evidence of ram pressure stripping is again limited to galaxy clusters.

3 SUMMARY OF OBSERVATIONS

We compare our findings to a recent survey of early-type galaxies from the SDSS (York et al. 2000) Spectroscopic Main Galaxy Survey (Strauss et al. 2002) Data Release 6 (Adelman-McCarthy et al. 2008). The sample of galaxies is described in Graves et al. (2009a,b). The galaxies selected were observed in the redshift range $0.04 < z < 0.08$, with light profiles that were both centrally concentrated and fit a de Vaucouleurs profile. To prevent a small proportion of young stars from biasing the measured luminosity, G09 excluded actively star-forming galaxies. Using colours and emission-line intensities, G09 also rejected Seyfert hosts, low-ionization nuclear emission-line region hosts, and transition objects, as they can host AGN which have been found to have light profiles intermediate between early and late types (Kauffmann et al. 2003).

Using the Lick indices (Worthey et al. 1994; Worthey & Ottaviani 1997) on 16 000 stacked spectra, G09 calculated mean luminosity-weighted ages and metallicities in bins with residual surface brightness above, within, and below the FP. The bins covered the approximate range $(0.0 < \log(R_{\rm e}/{\rm kpc}) < 0.7)$, $(1.9 < \log(\sigma/{\rm km\ s^{-1}}) < 2.4)$, and $-0.3 < \Delta \log(I_{\rm e}/{\rm L_\odot\ pc^{-2}}) < 0.3$, where $\Delta \log I_{\rm e}$ is the residual surface brightness resulting from a log fit in radius and velocity dispersion (Graves et al. 2010),

$$\log \frac{I_{\rm e}}{{\rm L_\odot\ pc^{-2}}} = -1.21 \log \frac{R_{\rm e}}{\rm kpc} + 1.16 \log \frac{\sigma}{\rm km\ s^{-1}} + 0.55. \quad (4)$$

We note that single stellar population (SSP) ages derived from Lick indices, as in G09, have been shown to be biased towards the most recent episode of star formation, resulting in age estimates that are systematically lower than the 'true' luminosity-weighted age (Trager & Somerville 2009).

G09 formed contours relating the mean light-weighted age and light-weighted metallicities, [Fe/H], [Mg/H], and [Mg/Fe], to effective radius and velocity dispersion across three slices of the face-on projection FP. While a different version of the S08/S12 SAM does include a more sophisticated chemical evolution model that discards the instantaneous recycling approximation and tracks contributions from different elements (Arrigoni et al. 2010), in this work we use a simplified instantaneous recycling chemical evolution model that tracks only the total metallicity Z and does not include the contribution from Type I supernovae (see section 2.5 of P14 for details). We thus consider the SAM metallicity to be most similar to [Mg/H], a measure of α-type enrichment.

The relevant results can be seen in figs 7 and 9 of G09. The authors found that stellar population age and metallicity are nearly independent of effective radius but strongly correlated with velocity dispersion. An analysis of the 6dFGS, which has a wider fibre aperture than SDSS, found similar correlations (Magoulas et al. 2012; Springob et al. 2012). In all three slices of the FP, galaxies with larger σ had older ages and higher metallicities. Stellar population age was also inversely correlated with residual surface brightness, so that the youngest galaxies tend to fall above the FP, in agreement with earlier observations (Forbes et al. 1998; Terlevich & Forbes 2002). A key conclusion of a subsequent analysis (Graves & Faber 2010; Graves et al. 2010) was that these trends arise because of structural differences in galaxies. These papers speculated that galaxies below the FP may have had earlier truncation times and formed most of their stars early, while galaxies above the FP have more extended star formation histories.

4 RESULTS

4.1 Binning in the FP

We make use of 23 of the $(50\ h^{-1}{\rm Mpc})^3$ subvolumes of the Bolshoi simulation in this analysis. We attempt to select a sample of low-redshift passive spheroid-dominated galaxies that is as similar as possible to the G09 sample. In order to do this, we select galaxies with stellar mass $B/T > 0.5$, specific star formation

rates less than 0.1 $M_\odot$ yr^{-1}/10^{11} $M_\odot$, and r-band absolute magnitudes $M_r > -19.0$ (the G09 50 per cent completeness threshold is $M_r = -19.7$). Making these selection cuts, we obtain a sample of 4342 model galaxies.

We note that the population of simulated galaxies consists solely of spheroid-dominated galaxies that have formed their spheroids via mergers or disc instabilities; this may not exactly correspond to the population of observed early-type galaxies. Based on an analysis of the SDSS, Cheng et al. (2011) have shown that a sample of passive, red sequence galaxies selected based on an apparent $B/T > 0.5$ (similar to the G09 sample) may actually contain a significant fraction of disc-dominated (passive S0 and Sa) galaxies. These galaxies might be created via environmental processes such as ram pressure stripping that are not included in our model. We have made no attempt to exclude galaxies that the SAMs characterize as having ('bright mode') AGN at redshift zero; G09 excluded Seyferts from their sample to avoid contamination of the spectra with emission lines, but as long as the structural properties of AGN are no different from inactive galaxies, this should not induce a bias. While the results presented here are for galaxies at redshift zero, we have also checked that including galaxies from the range $0 < z < 0.08$ does not significantly change the results.

We then separate our 'early-type' sample into three regimes according to their location perpendicularly above or below (i.e. 'through') the FP, using surface brightness as the independent variable. Surface brightness is calculated for our SAM galaxies via the luminosity given by stellar population synthesis models. Since we intend to compare to the G09 results, only galaxies that fall within the G09 range of radius, $(0.0 < \log(R_e/\mathrm{kpc}) < 0.7)$ and velocity dispersion, $(2.0 < \log(\sigma/\mathrm{km\ s^{-1}}) < 2.4)$ at redshift zero, are included in the fitting routine. We use a least-squares fit to determine a relation between (log) R_e, (log) σ, and (log) I_e, finding the FP prediction

$$\log \frac{I_e}{\mathrm{L_\odot\ pc^{-2}}} = -1.59 \log \frac{R_e}{\mathrm{kpc}} + 1.65 \log \frac{\sigma}{\mathrm{km\ s^{-1}}} - 0.49. \quad (5)$$

For each galaxy, the predicted surface brightness is determined using the above relation, and galaxies are separated by their residuals $\Delta \log(I_e/\mathrm{L_\odot\ pc^{-2}})$. Residuals in the three ranges [−0.3,−0.1], [−0.1,0.1], and [0.1,0.3] are, respectively, termed the low, mid, and high FP. Galaxies 'above' the FP have higher surface brightnesses than one would predict using their effective radii and velocity dispersions, while galaxies 'below' the FP have lower surface brightnesses. Galaxies with residuals outside the range [−0.3,0.3] are excluded. If we plot the simulated galaxies according to their location in FP-space, 90.2 per cent of the galaxies fall within the low-to-high FP slices (Fig. 1).

After separating the galaxies by their location within the FP, we place them in bins according to their radius and velocity dispersion just as G09 did for SDSS galaxies. We define this face-on projection in R_e and σ to be 'across' the FP. We then calculate the median age and metallicity for all galaxies within each bin, discarding bins with fewer than five galaxies. These values are used to form contours relating the stellar population parameters, namely age and metallicity, with the FP parameters and residuals. We caution that the simulated quantities are mass-weighted, while G09 calculates light-weighted ages, metallicities, and effective radii.

Comparing the P14 SAM and G09 observed populations, we find that they occupy slightly different regions of the R_e–σ parameter space (Fig. 2). The SAM includes a population of galaxies with low radii and low surface brightnesses that is not seen in G09. These galaxies tend to have low stellar masses and absolute magnitudes, and fall below the G09 completeness threshold.

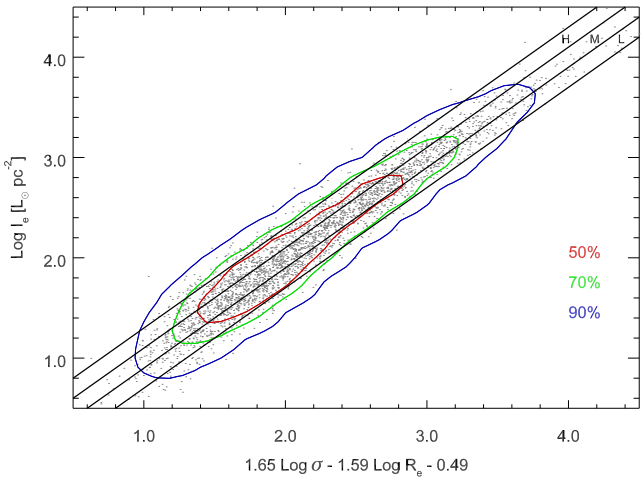

Figure 1. Distribution of simulated galaxies through the thickness of the FP. Galaxies are fit to a linear relation (horizontal axis) relating surface brightness with velocity dispersion and radius. The measured surface brightnesses are then plotted against the expected values. The areas between the solid black lines represent the slices we term the 'low-FP' (L), 'mid-plane' (M), and 'high-FP' (H), from bottom to top, according to the residual in surface brightness. Each slice has a thickness of 0.2. 90.2 per cent of the galaxies fall within the middle three FP slices. The red, green, and blue contours enclose 50, 70, and 90 per cent of all galaxies, while the grey points represent individual galaxies.

Our major findings are the contours seen in the upper panels of Figs 3 and 4. Stellar population age is positively correlated with velocity dispersion and is only weakly dependent on radius. We note that the parameter space has a much larger range in radius than velocity dispersion, so that while the contours appear nearly vertical, the radial dependence is non-negligible. If we consider the entire FP, the correlation between stellar age and effective radius has a Spearman rank coefficient $\rho = 0.03$ indicating nearly no correlation (Fig. 5). The relationship between age and velocity dispersion is much stronger, with a Spearman rank coefficient $\rho = 0.74$. Looking through the thickness of the FP, galaxies that lie above the FP (those with the largest residuals in $\log I_e$) have younger ages, as found by several observational studies (Forbes et al. 1998; Terlevich & Forbes 2002; G09). Galaxies above the FP have a mean age of 10.02 ± 1.61 Gyr, as compared to 12.12 ± 1.12 Gyr for galaxies below the FP.

If we compare the metallicity contours, the differences between the SAM and observations are more pronounced. In the simulated galaxies, metallicity increases strongly with velocity dispersion ($\rho = 0.83$) and weakly with effective radius ($\rho = 0.36$), whereas the G09 galaxies show very little dependence of metallicity on effective radius. The predicted dependence on effective radius is strongest for galaxies above the FP. As in G09, galaxies that lie above the FP do tend to have higher metallicities ($[Z] = 0.11 \pm 0.52$ versus $[Z] = 0.01 \pm 0.17$ for high-FP and low-FP galaxies, respectively).

4.2 Analysis of the age and metallicity trends

The strong correlation between metallicity and velocity dispersion in the SAM is not unexpected; it arises from the dependence on galaxy circular velocity of the gas and metal ejection rate due to stellar feedback (see S08 and P14). In fact the scatter in the

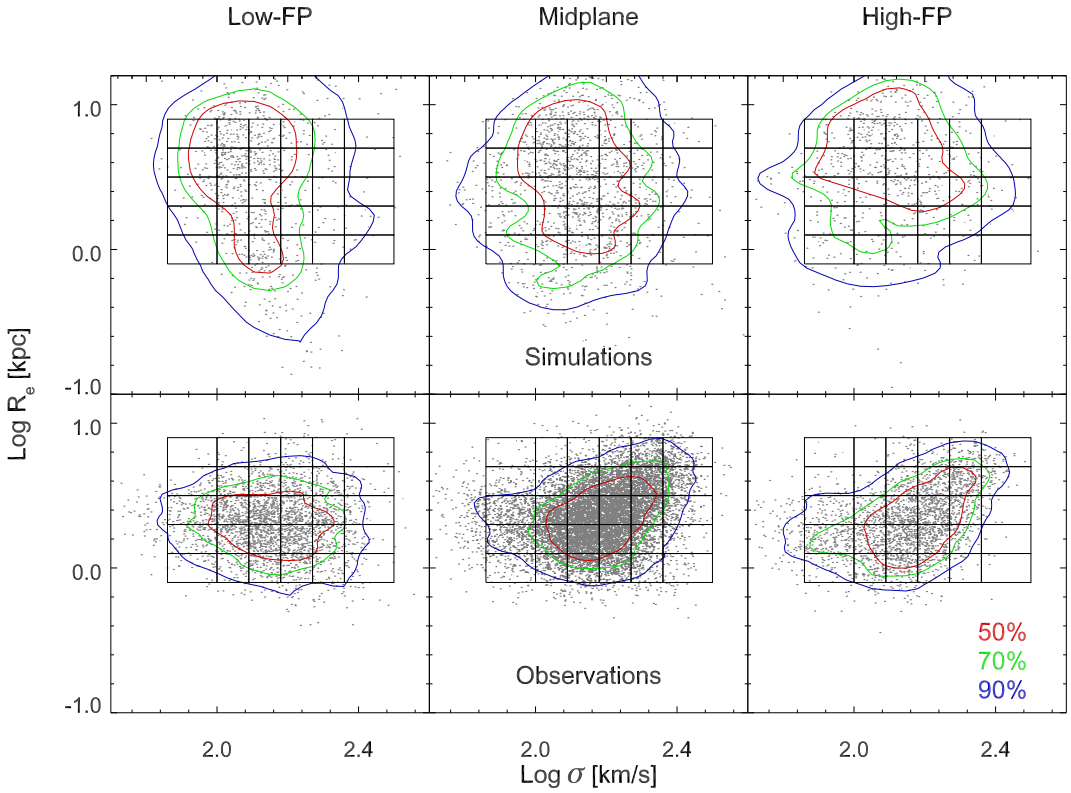

Figure 2. Distribution of radius and velocity dispersion for galaxies within each slice of the FP for the P14 SAM (top) and G09 observations (bottom). From left to right, the panels represent the 'low-FP', 'mid-plane', and 'high-FP' slices. The grid lines show the bin definitions in the region of the G09 observations; the median age and metallicities are calculated within each bin. The SAM contains a population of galaxies with low radii and low surface brightnesses that fall below the completeness threshold of the G09 survey. The red, green, and blue contours enclose 50, 70, and 90 per cent of galaxies meeting our selection criteria, while the grey points represent individual galaxies.

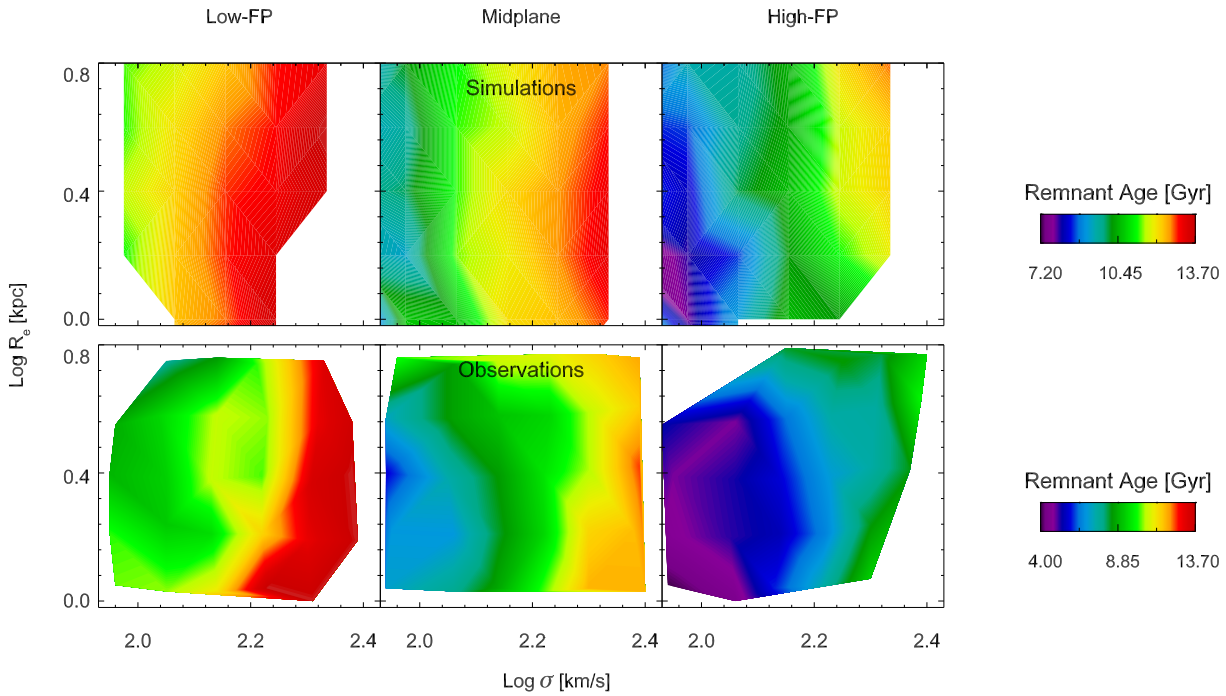

Figure 3. Relation between mass-weighted age, effective radius, and velocity dispersion for early-type galaxies in the P14 SAM (top) and G09 observations (bottom). Here, we plot only the region considered in G09. The different panels represent the three central slices of the FP, as shown in Fig. 2. In the SAM and the observations, stellar population age increases with velocity dispersion, but the SAM galaxies display a narrower range in age. Galaxies that lie above the FP also tend to be younger than those that lie below the FP.

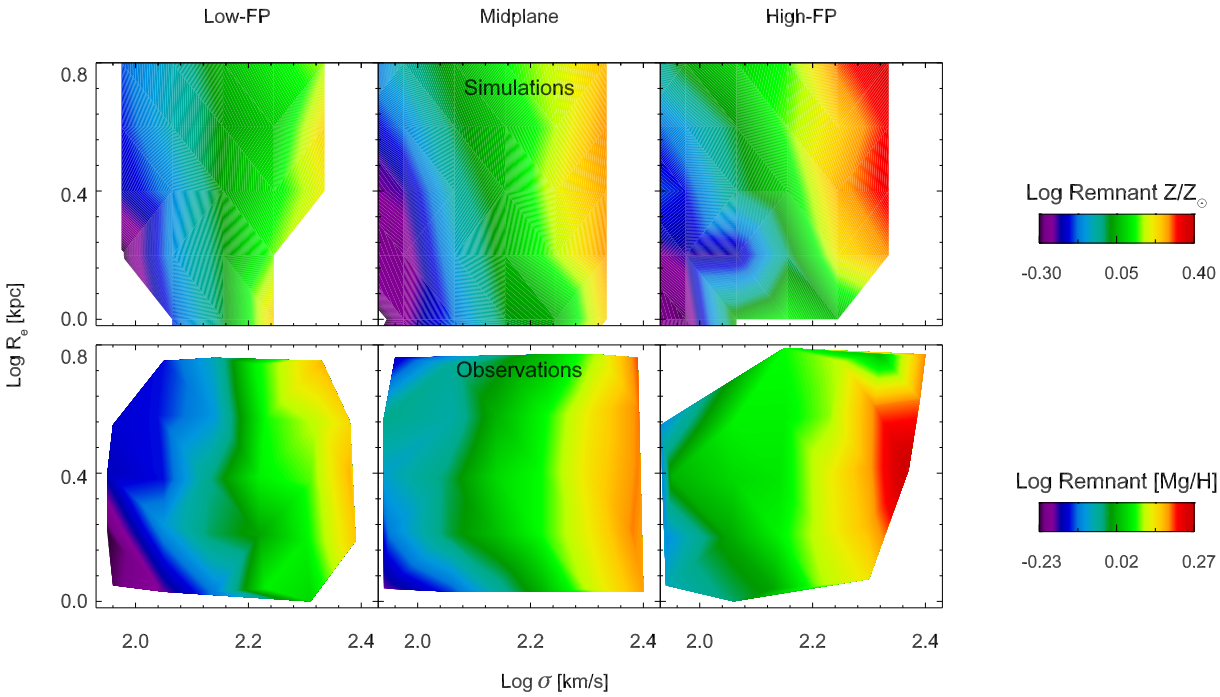

Figure 4. Relation between mass-weighted metallicity, effective radius, and velocity dispersion for early-type galaxies in the P14 SAM (top) and G09 observations (bottom). Here, we plot only the region considered in G09. The different panels represent the three central slices of the FP, as shown in Fig. 2. While [Mg/H] depends strongly on velocity dispersion in G09, in the SAM metallicity depends on both velocity dispersion and effective radius. The simulated galaxies tend to have slightly lower metallicities than observations on average.

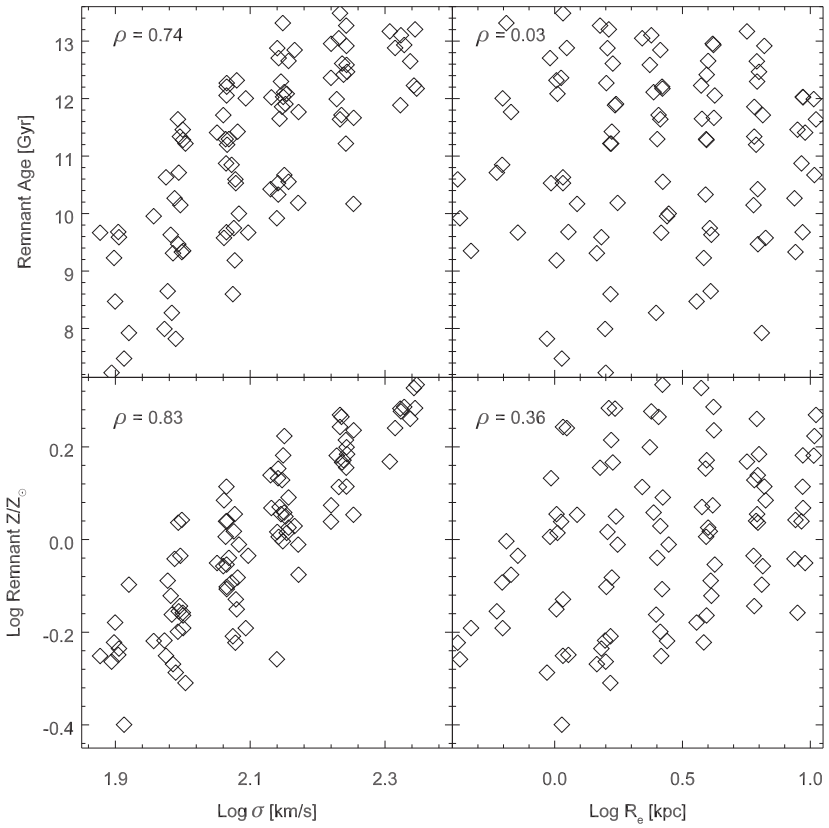

Figure 5. Predicted relation between mass-weighted age (top) and metallicity (bottom), velocity dispersion (left) and effective radius (right), for each of the bins in the FP, for the P14 SAM. Each panel shows the Spearman rank coefficient ρ indicating the strength of the two-dimensional relation. Both age and metallicity are strong functions of velocity dispersion. Age is nearly independent of effective radius, while metallicity weakly increases with effective radius.

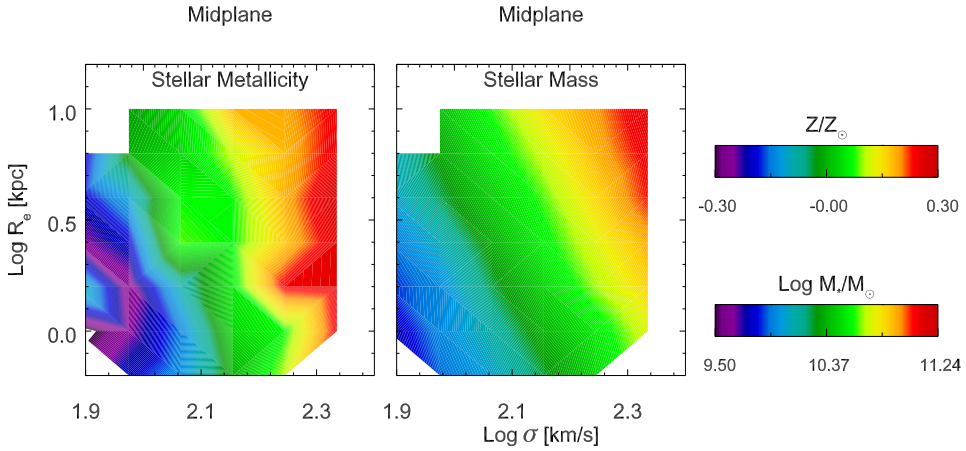

Figure 6. Relation between mass-weighted metallicity (left) and stellar mass (right), effective radius, and velocity dispersion for early-type galaxies in the P14 SAM. Both panels represent the middle slice of the FP, as shown in Fig. 2. Colours are individually normalized. Since the SAM predicts a very strong correlation between stellar mass and metallicity, the two trends are nearly identical.

mass–metallicity relationship predicted by the SAM for the whole galaxy population is much smaller than that measured by Gallazzi et al. (2005) for low-mass galaxies, though a smaller scatter is obtained in other observational studies using more direct metallicity indicators (Woo, Courteau & Dekel 2008; Kirby et al. 2010).

If we consider that stellar mass is closely related to the dynamical mass, which is in turn proportional to $\sigma^2 r$ then the implications of the upper panels of Figs 3 and 4 become clearer: the tight mass–metallicity relationship is reflected in a dependence of metallicity on both effective radius and velocity dispersion in the projected FP. In fact, when stellar mass and metallicity are plotted alongside each other in the middle slice of the FP (Fig. 6), we find that the trends are similar, although metallicity is relatively independent of R_e at high σ, whereas higher R_e galaxies have higher stellar masses at high σ. As we will show, galaxies above the FP have the lowest concentrations of DM within their effective radii, making the dependence on stellar mass even more pronounced.

We next discuss the simulated age–FP trend, which shows better agreement with observations than might have been expected. We note that, in the model, the velocity dispersion is calculated from both the effective radius and the total mass within that radius; thus velocity dispersion and effective radius are intrinsically linked. However, the ages of the simulated galaxies have a clear dependence on the former and less dependence on the latter. As we will discuss in Section 5.1, minor mergers are mainly responsible for blurring any correlation between age and effective radius while preserving the relation between age and velocity dispersion.

4.3 Comparison to observations

To compare with G09, we have replotted the age and metallicity contours over the range $(0.0 < \log(R_e/\mathrm{kpc}) < 0.7)$, $(1.9 < \log(\sigma/\mathrm{km\ s^{-1}}) < 2.4)$, and $-0.3 < \Delta \log(I_e/\mathrm{L}_\odot\ \mathrm{pc}^{-2}) < 0.3$ considered by G09 alongside the G09 data (Figs 3 and 4). We caution that the G09 ages were later found to be systematically high by ∼0.12 dex, owing to weak emission in the Hβ absorption line (Graves & Faber 2010); however, this should not affect the overall trends. We also note that we calculate mass-weighted ages and metallicities while G09 calculated SSP ages and metallicites using the Lick indices. These SSP quantities have been shown to more closely correlate with the epoch of most recent star formation, and result in ages that are systematically younger than mass-weighted and light-weighted ages (Trager & Somerville 2009).

Examining the trends within FP slices, the age–FP correlations are in rough agreement with G09. The major difference between our results and those of G09 is that we find metallicity to be dependent on radius and velocity dispersion, especially above the FP, while G09 found metallicity to be dependent on velocity dispersion alone. The SAM does a better job of reproducing the observed trends through, as opposed to across, the FP. Galaxies that fall above the FP tend to be younger and more metal-enhanced than average, while those that fall below the FP are older and more metal-poor, in agreement with G09.

5 DISCUSSION

Having established the major trends of age and metallicity through the thickness of the FP, we can now attempt to characterize the significance of these trends. A key question is how much of the variation through the FP arises from structural differences in galaxies as compared to the passive fading of elliptical galaxies. If galaxies do 'settle' on to the FP over time, we might expect galaxies above the FP to have younger ages and higher metallicities, in agreement with both simulations and observations. However, this process would not explain why age and metallicity appear to be more strongly correlated with velocity dispersion than effective radius. In addition, this would not explain the significant overlap in age and metallicity ranges in the three FP slices.

5.1 Analysis of trends across the FP

In order to understand all of these trends simultaneously, it is necessary to study the implications of our prescription for effective radius and velocity dispersion. In our model, a galaxy's effective radius and velocity dispersion are tightly correlated, regardless of whether it forms a spheroid through a merger or through a disc instability event. As a population however, galaxies experience large changes in effective radius with redshift, but only moderate changes in velocity dispersion. By quantifying the scatter introduced by these evolutionary processes, we can attempt to explain how low-redshift galaxies with similar ages and metallicities have similar velocity dispersions but a range of effective radii.

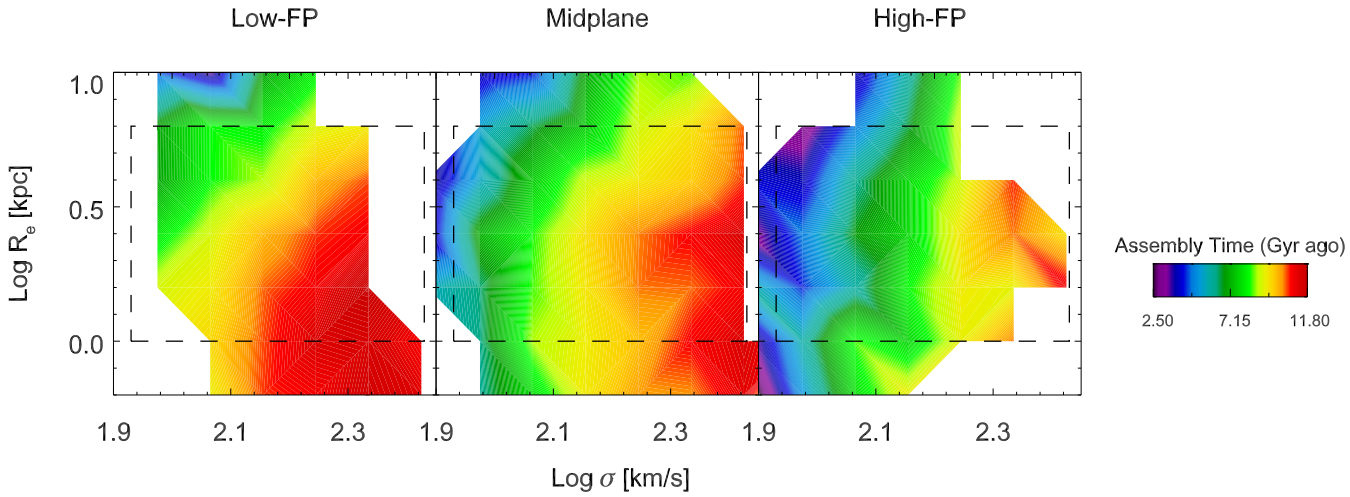

Figure 7. Relation between the time since the galaxy was assembled (became spheroid dominated), effective radius, and velocity dispersion for early-type galaxies. The different panels represent the three central slices of the FP, as shown in Fig. 2. Early-type galaxies that were assembled earlier have higher velocity dispersions and tend to fall below the FP.

Recent works (Naab et al. 2009; Hopkins et al. 2010; Oser et al. 2012) have suggested that gas-poor minor mergers may produce at least some of the observed evolution in the size–mass relation for early-type galaxies, forming an evolutionary link between the compact galaxies seen at high redshifts and the more diffuse galaxies seen in the local universe. While there is some question as to whether the merger rate is sufficient to explain all of the size evolution (Trujillo, Ferreras & de la Rosa 2011; Newman et al. 2012; Nipoti et al. 2012; Quilis & Trujillo 2012), we can predict the effect that these events would have on the population.

It is important to note that in our model, following the behaviour in the numerical simulations, any merger where one or both of the progenitors is spheroid dominated is treated as a dissipationless event, as we explained in Section 2.2. Thus, mergers between a massive compact elliptical and a smaller galaxy can be expected to significantly increase the size of the remnant galaxy. Using conservation of energy and the virial theorem, Naab et al. (2009) show that for a series of minor mergers that increase the mass of the galaxy from M_i to M_f, the radius increases as $(M_f/M_i)^2$ while the velocity dispersion decreases as $(M_f/M_i)^{-1/2}$. These scaling relations necessarily introduce a large amount of scatter in effective radius: if, for example, two identical galaxies increase their masses by a factor of 1.9 and 2.0, respectively, their resulting radii will differ by 9.8 per cent while their velocity dispersions will only differ by 2.6 per cent.

This large amount of variation in effective radius means that any original correlations between effective radius and age or metallicity will be weakened by a series of minor mergers. It is interesting to note that this model predicts that there may be a stronger dependence of stellar population parameters on effective radius at higher redshifts, where the effects of minor mergers are less prevalent.

A second major implication of these scaling relations is that the velocity dispersion of a galaxy should remain relatively unchanged from its formation to the present day; if anything, it should decrease slightly. This prediction is in agreement with both cosmological simulations (Oser et al. 2012) and observational evidence that the velocity dispersion function evolves to higher values at higher redshifts but at a rate much slower than the evolution in the size–mass relation (Cenarro & Trujillo 2009; Bezanson et al. 2011).

Since our SAM, based on the Bolshoi simulation merger trees, contains the detailed merger history of every simulated galaxy, we are able to test this prediction directly. If we define the 'assembly time' as the time a galaxy most recently became spheroid dominated ($B/T > 0.5$), we can examine its variation across and through the FP using the same method as described earlier for age and metallicity. The results can be seen in Fig. 7. As expected, galaxies with higher velocity dispersions tend to have assembled earlier. Thus, a galaxy's velocity dispersion may be a key indicator relating its current structure to the epoch of its formation.

Fig. 7 also shows that galaxies below the FP tend to have earlier assembly times. There is a significant amount of overlap in this correlation; however, in particular the galaxies with the highest velocity dispersions have similar high formation times for all three slices of the FP. This indicates that a further process must be invoked to explain the trends through the thickness of the FP.

5.2 Analysis of trends through the FP

Stellar population trends through the thickness of the FP can arise in a number of different ways; any process that increases the dynamical mass-to-light ratio of a galaxy will move it further below the virial plane. Graves & Faber (2010) provide a decomposition of the deviation from the virial theorem, separating it into four components.

(i) The ratio of the estimated dynamical mass to the true mass within one R_e.
(ii) The ratio of the true mass within one R_e to the projected stellar mass.
(iii) The ratio of the projected stellar mass within one R_e to the stellar mass computed with an assumed IMF.
(iv) The stellar mass-to-light ratio for the assumed IMF.

For the simulated galaxies and their corresponding FP, the first and third terms are identically one, as we have no uncertainty in the dynamical mass estimate and we model and 'observe' galaxies using the same IMF. Since we know the stellar mass-to-light ratio for the galaxies and can calculate the central DMF (see below), we may calculate the second and fourth terms directly. We note that if our assumed Chabrier IMF is incorrect, or if the IMF is non-universal (Conroy & van Dokkum 2012; Dutton, Mendel & Simard 2012;

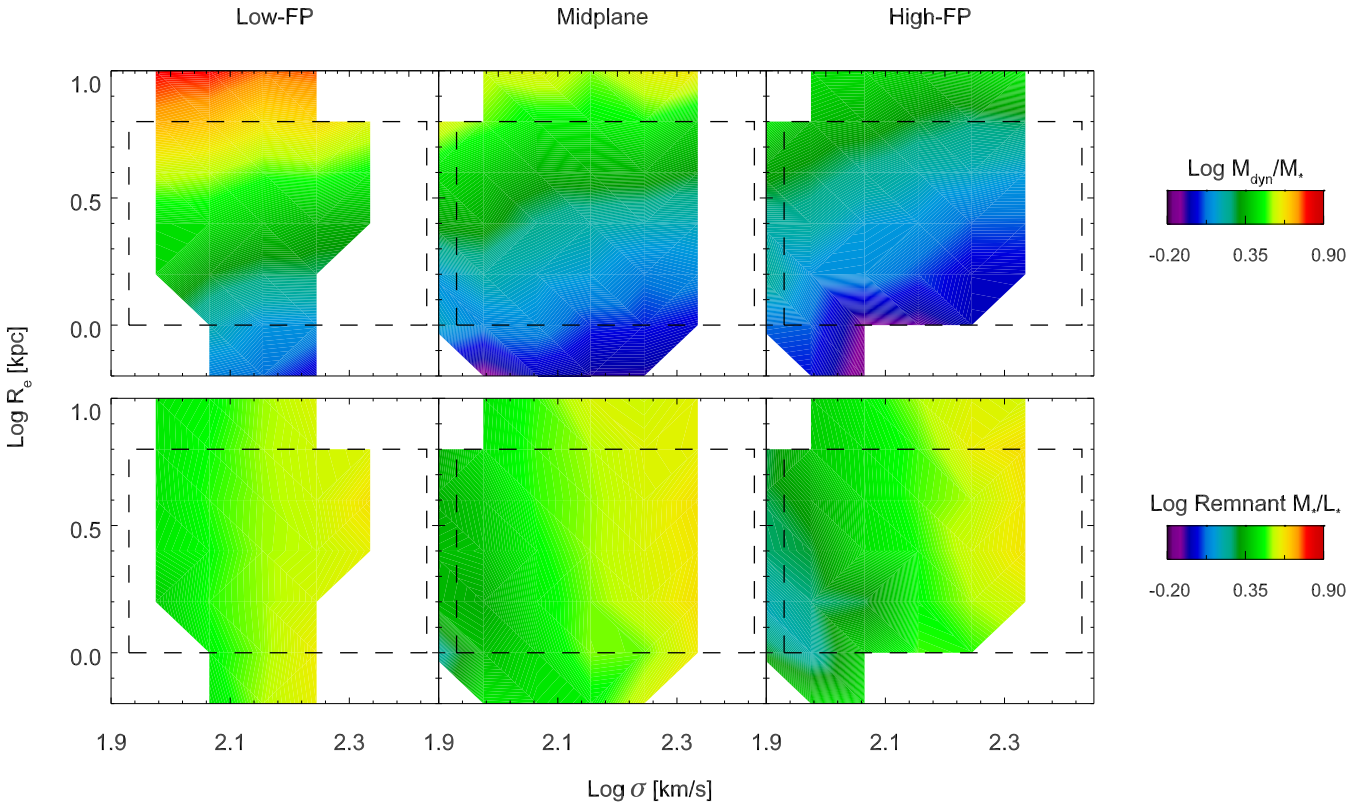

Figure 8. Relation between dynamical-to-stellar mass ratio (top), stellar mass-to-light ratio (bottom), effective radius, and velocity dispersion for early-type galaxies in the P14 SAM. The different panels represent the three central slices of the FP, as shown in Fig. 2. The grey dashed line indicates the region analysed in G09. Galaxies that fall below the FP have higher dynamical-to-stellar masses and mass-to-light ratios. The variation in dynamical-to-stellar mass through the FP is much larger than the variation in the mass-to-light ratio (note that both relations use the same colour scalings).

Spiniello et al. 2012) the fourth term would change; we discuss the implications of a non-universal IMF later in this section.

We have used the same process as described above to project the dynamical-to-stellar mass and stellar mass-to-light ratios of early-type galaxies across (i.e. along the face-on projection) and through the FP (Fig. 8). The results regarding variations through the FP are in agreement with the conclusions of Graves & Faber (2010): galaxies that fall below (above) the FP have higher (lower) dynamical-to-stellar mass ratios and slightly higher (lower) stellar mass-to-light ratios, at fixed velocity dispersion and R_e. Stated another way, galaxies below the FP have lower stellar masses and central surface densities at fixed R_e. The variations in stellar mass-to-light ratio are due to differences in the stellar populations: since galaxies above the FP are younger than galaxies below the FP, they have more young stars and hence lower stellar mass-to-light ratios. The variations in the central DMF reflect structural differences in the density profiles of galaxies and DM haloes.

Comparing the trends through the thickness of the FP, at fixed R_e and σ the dynamical-to-stellar mass ratio has a much larger degree of variation than the stellar mass-to-light ratio. If we limit our analysis to bins of R_e and σ that have at least five galaxies in each slice of the FP, we find that the average variance in the DMF contributes 94 per cent of the thickness of the FP, while the stellar mass-to-light ratio only contributes 6 per cent. This is in general agreement with Graves & Faber (2010), who found that the DMF and IMF variation have a combined contribution in the range of 47–98 per cent, and that measured variations in the stellar mass-to-light ratio were insufficient to explain all of the thickness of the FP. This is another indication that underlying structural differences, as opposed to passive fading, are the main contributors to the thickness of the FP.

We note that our model assumes that all stars formed under a Chabrier IMF. There is mounting evidence, however, that the IMF may be non-universal. Early-type galaxies and spheroids with high stellar masses or velocity dispersions in the local universe may follow a 'bottom-heavy' IMF, with more low-mass stars (Conroy & van Dokkum 2012; Dutton et al. 2012; Spiniello et al. 2012). While there is some disagreement as to the slope of this bottom-heavy IMF, an IMF that varies with velocity dispersion would contribute to the thickness of the simulated FP; galaxies below the FP with high-velocity dispersions would have higher stellar mass-to-light ratios, moving them even further below the FP. Thus while our results through the FP are consistent with those of Graves & Faber (2010), we have not accounted for any contributions from a varying IMF in this work. Regarding the variation in M_*/L and $M_{\rm dyn}/M_*$ across the FP, we note that although Graves & Faber (2010) find that M_*/L varies with σ and is nearly independent of R_e in agreement with Fig. 8 (bottom), they find that $M_{\rm dyn}/M_*$ increases with both R_e and σ while in Fig. 8 (top) we find that $M_{\rm dyn}/M_*$ mainly increases with increasing R_e, with $M_{\rm dyn}/M_*$ slightly decreasing with increasing σ.

To summarize our results through the FP so far, we have found that galaxies below the FP tend to be old and metal poor. They became spheroid-dominated at early times, and have high dynamical-to-stellar mass ratios at a given R_e and σ. In contrast, galaxies above the FP tend to be young and metal rich, with later formation times and relatively high stellar masses at fixed R_e and σ. In an analysis of the trends found in G09 and Graves & Faber (2010), Graves et al. (2010) found these results could be explained by a

Table 1. Parameters used to determine the mass assembly histories of early-type galaxies. The low-FP, mid-plane, and high-FP values are the mean of each parameter for early-type galaxies in each plane.

Parameter	Description	Low-FP	Mid-plane	High-FP
Assembly time (Gyr ago)	Time when the galaxy most recently became spheroid-dominated ($B/T > 0.5$)	9.10 ± 2.29	8.35 ± 2.62	6.65 ± 3.30
Formation time (Gyr ago)	Time by which 1/2 of the stars in a galaxy formed	10.88 ± 0.77	10.34 ± 0.97	9.28 ± 1.37
Star formation duration (Gyr)	Time to form the middle 68 per cent of a galaxy's stars	2.32 ± 0.93	2.82 ± 1.04	3.94 ± 1.29

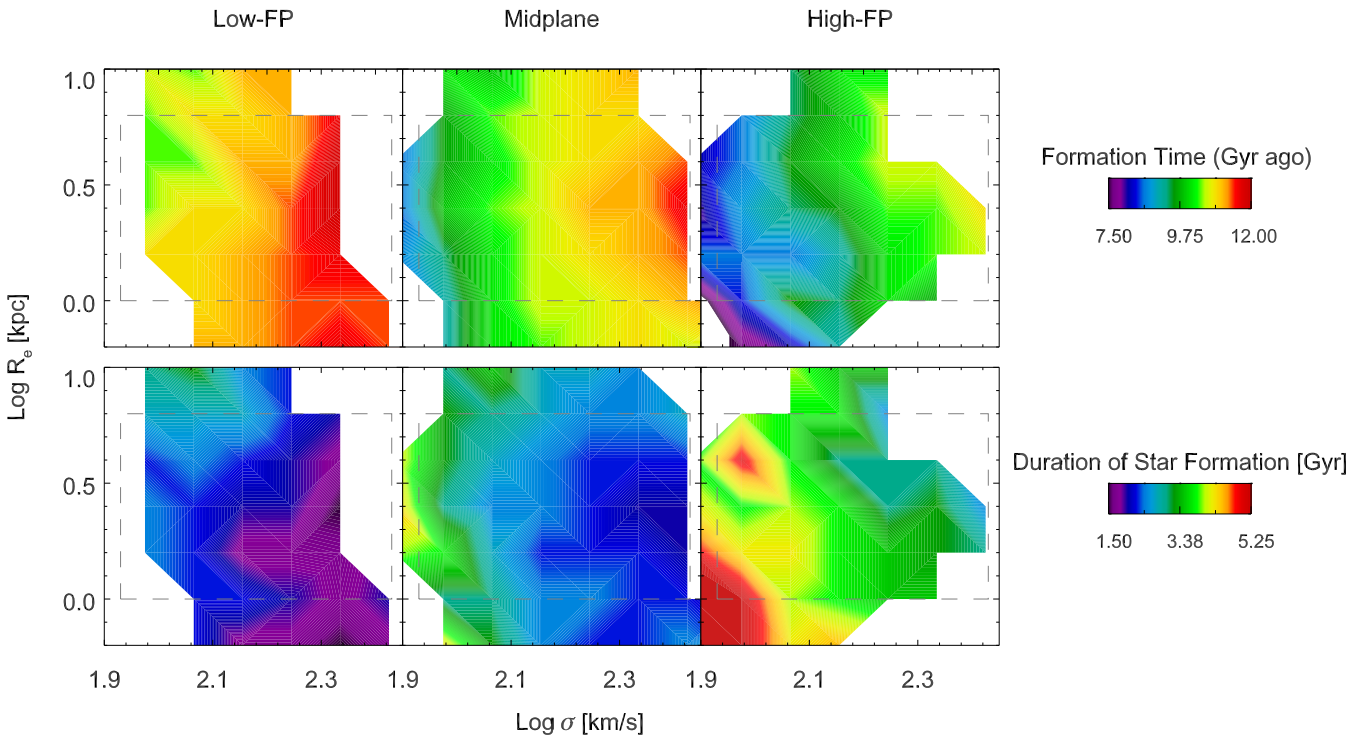

Figure 9. Relation between the formation time (top), duration of star formation (bottom), effective radius, and velocity dispersion for early-type galaxies in the P14 SAM. The different panels represent the three central slices of the FP, as shown in Fig. 2. The grey dashed line indicates the region analysed in G09. Galaxies below the FP tend to have formed their stars early and have short star formation time-scales. Galaxies above the FP have extended star formation histories and formed their stars more recently.

scenario in which galaxies below the FP have their star formation truncated at early times, while those above the FP have more extended star formation histories. Since the SAM contains information about the star formation histories for every galaxy, we can test this scenario.

The P14 SAM keeps track of the star formation history of each galaxy, divided into 196 log-spaced bins in age. For this analysis, we have defined the 'star formation duration' as the duration over which each galaxy formed the middle 68 per cent of its stars. Thus galaxies with a wider distribution of stellar ages will have longer star formation durations. We have defined 'formation time' as the time by which half of the stars in the galaxy have formed; this quantity is significant because it incorporates information about the stars that formed in situ in the galaxy as well as those that were accreted. Taken together, the 'assembly time' (Fig. 7) and the 'formation time' provide a link between the structure of a galaxy and the properties of its stellar population. These definitions are summarized in Table 1. We have plotted the correlations between star formation duration and formation time, effective radius, and velocity dispersion for all three FP slices in Fig. 9. Comparing the relations, it is evident that galaxies below the FP have early formation times and short star formation time-scales; in fact roughly 75 per cent of these galaxies have star formation time-scales less than 2 Gyr. Galaxies above the FP formed their stars slightly later, but more significantly, they have much longer star formation time-scales; 70 per cent of these galaxies have star formation durations *greater* than 2 Gyr.

The long duration of star formation allows for more conversion of gas to stars, decreasing the dynamical-to-stellar mass ratio. As we established earlier that variations in the mass-to-light ratio cannot account for most of the thickness of the FP, these galaxies will not 'fall' on to the FP over time. Their assembly histories have produced galaxies with high baryon fractions and high stellar central surface densities, and their relatively recent star formation has produced stellar populations with young ages and high metallicities. This result is a key prediction of our model: the thickness of the FP appears to be due to structural differences in the galaxies resulting from their differing formation histories. Previous works (e.g. Wechsler et al. 2002) have linked the $z = 0$ concentrations of DM haloes with the duration and epoch of mass assembly; here, we find similar results for early-type galaxies.

Finally, we can combine these relations to account for both the structural and the stellar population differences through the FP. Galaxies below the FP became spheroid dominated early, in a regime in which stellar velocity dispersions were higher at fixed

stellar mass. This may also account for the compact tail of galaxies seen in the low-FP pane Fig. 2. These galaxies formed their stars and quenched early, leaving them with old ages, low metallicities, and structural properties that are perhaps representative of compact ellipticals at higher redshifts.

In contrast, galaxies above the FP became spheroid dominated and formed their stars slightly later. More importantly, they have extended star formation histories, producing galaxies with younger ages and higher metallicities. While they do have slightly lower stellar mass-to-light ratios, most of the variation in residual surface brightness stems from their high central stellar surface densities and low DMFs.

6 CONCLUSIONS

We have used the Santa Cruz SAM (S08; S12; P14) along with an analytic model for computing the size and velocity dispersion of stellar spheroids from C08, C11 and Guo et al. (2011) to predict the distribution of stellar ages and metallicities for early-type galaxies across and through the FP. We allow the model to run self-consistently to redshift zero, at which point we select quiescent spheroid-dominated galaxies. We then separate them according to their residual surface brightness in the FP and calculate the mass-weighted ages and metallicities as a function of effective radius and velocity dispersion.

In agreement with G09 and an analysis of the 6dFGRS (Magoulas et al. 2012; Springob et al. 2012), we find that stellar ages increase as a strong function of velocity dispersion and are nearly independent of radius. We predict that the strong correlation with velocity dispersion stems from the fact that the velocity dispersion of the galaxy changes little from its formation to the present day, even in the face of minor mergers. Meanwhile minor mergers and ongoing disc instabilities introduce large amounts of variation in the radius over time, washing out correlations with effective radius.

We show that galaxies with higher residual surface brightness ('above' the FP) tend to be younger and more metal rich. Examining their structural properties, we find them to have lower stellar mass-to-light ratios and lower dynamical-to-stellar mass ratios. These galaxies became spheroid-dominated relatively recently and formed their stars later than galaxies below the FP. Furthermore these galaxies have extended star formation histories, allowing for a more complete conversion of gas to stars and for the production of young, metal-rich stars. These results are in close agreement with the observational analysis of Graves et al. (2010), which also showed a correlation between the chemical abundance of α elements, the duration of star formation, and velocity dispersion. A different version of the Somerville et al. SAM contains a detailed Galactic Chemical Evolution model, including non-instantaneous recycling, enrichment by both core collapse and Type Ia supernovae, and tracking of multiple chemical elements, as described in Arrigoni et al. (2010). This version of the SAM was shown to reproduce the observed scaling between [α/Fe] and velocity dispersion, suggesting that our model would also reproduce the observed correlations between [α/Fe], the duration of star formation, and residual surface brightness, as found in Graves et al. (2010). We plan to pursue this further in future work. Note that Yates et al. (2013) also found a correlation between stellar mass and [α/Fe] for early-type galaxies in a SAM, without any modification to the IMF. Differences in star formation time-scale were also found to be a key cause in that work.

We find that variations in the stellar mass-to-light ratio and the DMF within one effective radius both contribute to the thickness of the FP, with the DMF having a much larger effect. Thus, we predict that the thickness of the FP is largely due to structural differences between galaxies, rather than stellar population differences. Galaxies above the FP have higher ratios of stellar-to-dark matter within one effective radius; put another way, at fixed halo mass, galaxies above the FP have had more efficient star formation. This result is also in agreement with the conclusions of G09, although we have not allowed for any contribution from a non-universal IMF. The reasonably good agreement of our SAM predictions with SDSS observations provides motivation to pursue more detailed modelling.

ACKNOWLEDGEMENTS

We thank Matthew Colless, Brad Holden, Patrik Jonsson, Mark Krumholz, Thorsten Naab, Ludwig Oser, Stefano Profumo, and Connie Rockosi for useful discussions, and we thank the anonymous referee for many helpful questions and suggestions. LAP thanks the Space Telescope Science Institute for support and hospitality. LAP and JRP were supported by NSF AST-1010033 and the CANDELS grant HST-GO-12060.12-A.

REFERENCES

Adelman-McCarthy J. K., Agüeros M. A., Allam S. S., Zehavi I., Zucker D. B., 2008, ApJS, 175, 297
Arrigoni M., Trager S. C., Somerville R. S., Gibson B. K., 2010, MNRAS, 402, 173
Barnes J. E., Hernquist L., 1996, AJ, 471, 115
Behroozi P. S., Wechsler R. H., Wu H.-Y., Busha M. T., Klypin A. A., Primack J. R., 2013, ApJ, 763, 18
Bell E. F., Zheng X. Z., Papovich C., Borch A., Wolf C., Meisenheimer K., 2007, ApJ, 663, 834
Bezanson R., van Dokkum P. G., Tal T., Marchesini D., Kriek M., Franx M., Coppi P., 2009, ApJ, 697, 1290
Bezanson R. et al., 2011, ApJ, 737, L31
Bournaud F. et al., 2011, ApJ, 730, 4
Bower R. G., Benson A. J., Malbon R., Helly J. C., Frenk C. S., Baugh C. M., Cole S., Lacey C. G., 2006, MNRAS, 370, 645
Bruzual G., Charlot S., 2003, MNRAS, 344, 1000
Cenarro A. J., Trujillo I., 2009, ApJ, 696, L43
Chabrier G., 2003, PASP, 115, 763
Cheng J. Y., Faber S. M., Simard L., Graves G. J., Lopez E. D., Yan R., Cooper M. C., 2011, MNRAS, 412, 727
Ciotti L., Lanzoni B., Volonteri M., 2007, ApJ, 658, 65
Cole S., Lacey C. G., Baugh C. M., Frenk C. S., 2000, MNRAS, 319, 168
Combes F., Debbasch F., Friedli D., Pfenniger D., 1990, A&A, 233, 82
Conroy C., van Dokkum P. G., 2012, ApJ, 760, 71
Covington M., Dekel A., Cox T. J., Jonsson P., Primack J. R., 2008, MNRAS, 384, 94 (C08)
Covington M. D., Primack J. R., Porter L. A., Croton D. J., Somerville R. S., Dekel A., 2011, MNRAS, 415, 1029 (C11)
Cox T. J., 2004, PhD thesis, Univ. California Santa Cruz
Cox T. J., Dutta S. N., Matteo T. D., Hernquist L., Hopkins P. F., Robertson B., Springel V., 2006, ApJ, 650, 791
Cox T. J., Jonsson P., Somerville R. S., Primack J. R., Dekel A., 2008, MNRAS, 384, 386
Croton D. J. et al., 2006, MNRAS, 365, 11
De Lucia G., Fontanot F., Wilman D., Monaco P., 2011, MNRAS, 414, 1439
Debattista V. P., Carollo C. M., Mayer L., Moore B., 2004, ApJ, 604, L93
Dekel A., Cox T. J., 2006, MNRAS, 370, 1445
Dekel A. et al., 2009, Nature, 457, 451
Dekel A., Zolotov A., Tweed D., Cacciato M., Ceverino D., Primack J. R., 2013, MNRAS, 435, 999
Djorgovski S., Davis M., 1987, ApJ, 313, 59

Dressler A., Lynden-Bell D., Burstein D., Davies R. L., Faber S. M., Terlevich R., Wegner G., 1987, ApJ, 313, 42
Dutton A. A., Mendel J. T., Simard L., 2012, MNRAS, 422, L33
Efstathiou G., Lake G., Negroponte J., 1982, MNRAS, 199, 1069
Faber S. M., Dressler A., Davies R. L., Burstein D., Lynden-Bell D., 1987, in Faber S. M., ed., Nearly Normal Galaxies: From the Planck Time to the Present. Springer-Verlag, New York, p. 175
Faber S. M. et al., 2007, ApJ, 665, 265
Fontanot F., De Lucia G., Monaco P., Somerville R. S., Santini P., 2009, MNRAS, 397, 1776
Forbes D. A., Ponman T. J., Brown R. J. N., 1998, ApJ, 508, L43
Gallazzi A., Charlot S., Brinchmann J., White S. D. M., Tremonti C. A., 2005, MNRAS, 362, 41
Graves G. J., Faber S. M., 2010, ApJ, 717, 803
Graves G. J., Faber S. M., Schiavon R. P., 2009a, ApJ, 693, 486
Graves G. J., Faber S. M., Schiavon R. P., 2009b, ApJ, 698, 1590 (G09)
Graves G. J., Faber S. M., Schiavon R. P., 2010, ApJ, 721, 278
Greene J. E., Murphy J. D., Comerford J. M., Gebhardt K., Adams J. J., 2012, ApJ, 750, 32
Guo Q. et al., 2011, MNRAS, 413, 101
Hilz M., Naab T., Ostriker J. P., 2013, MNRAS, 429, 2924
Hohl F., 1971, ApJ, 168, 343
Hopkins A. M., Beacom J. F., 2008, ApJ, 682, 1486
Hopkins P. F. et al., 2009a, MNRAS, 397, 802
Hopkins P. F., Cox T. J., Younger J. D., Hernquist L., 2009b, ApJ, 691, 1168
Hopkins P. F., Bundy K., Hernquist L., Wuyts S., Cox T. J., 2010, MNRAS, 401, 1099
Johansson P. H., Naab T., Burkert A., 2009, ApJ, 690, 802
Johansson P. H., Naab T., Ostriker J. P., 2012, ApJ, 754, 115
Jones D. H. et al., 2004, MNRAS, 355, 747
Jones D. H. et al., 2009, MNRAS, 399, 683
Jørgensen I., Franx M., Kjaergaard P., 1996, MNRAS, 280, 167
Jørgensen I., Chiboucas K., Flint K., Bergmann M., Barr J., Davies R., 2006, ApJ, 639, L9
Kauffmann G. et al., 2003, MNRAS, 341, 54
Khochfar S., Burkert A., 2003, ApJ, 597, L117
Khochfar S., Silk J., 2006, ApJ, 648, L21
Kirby E. N. et al., 2010, ApJS, 191, 352
Klypin A. A., Trujillo-Gomez S., Primack J., 2011, ApJ, 740, 102
Komatsu E. et al., 2009, ApJS, 180, 330
Komatsu E. et al., 2011, ApJS, 192, 18
Laporte C. F. P., White S. D. M., Naab T., Gao L., 2013, MNRAS, 435, 901
Magoulas C. et al., 2012, MNRAS, 427, 245
Mihos J. C., Hernquist L., 1994, ApJ, 437, L47
Naab T., Khochfar S., Burkert A., 2006, ApJ, 636, L81
Naab T., Johansson P. H., Ostriker J. P., 2009, ApJ, 699, L178
Navarro J. F., Frenk C. S., White S. D. M., 1996, ApJ, 462, 563
Nelan J. E., Smith R. J., Hudson M. J., Wegner G. A., Lucey J. R., Moore S. A. W., Quinney S. J., Suntzeff N. B., 2005, ApJ, 632, 137
Newman A. B., Ellis R. S., Bundy K., Treu T., 2012, ApJ, 746, 162
Nipoti C., Treu T., Leauthaud A., Bundy K., Newman A. B., Auger M. W., 2012, MNRAS, 422, 1714
Oser L., Naab T., Ostriker J. P., Johansson P. H., 2012, ApJ, 744, 63
Ostriker J. P., Peebles P. J. E., 1973, ApJ, 186, 467
Parry O. H., Eke V. R., Frenk C. S., 2009, MNRAS, 396, 1972
Porter L. A., Somerville R. S., Primack J. R., Johansson P. H., 2014, MNRAS, 444, 942 (P14)
Quilis V., Trujillo I., 2012, ApJ, 752, L19
Shankar F., Marulli F., Bernardi M., Mei S., Meert A., Vikram V., 2013, MNRAS, 428, 109
Smith R. J., Lucey J. R., Hudson M. J., 2007, MNRAS, 381, 1035
Somerville R. S., Hopkins P. F., Cox T. J., Robertson B. E., Hernquist L., 2008, MNRAS, 391, 481 (S08)
Somerville R. S., Gilmore R. C., Primack J. R., Domínguez A., 2012, MNRAS, 423, 1992 (S12)
Spiniello C., Trager S. C., Koopmans L. V. E., Chen Y. P., 2012, ApJ, 753, L32
Springob C. M. et al., 2012, MNRAS, 420, 2773
Strauss M. A., Weinberg D. H., Lupton R. H., Narayanan V. K., Annis J., Bernardi M., York D. G., Zehavi I., 2002, AJ, 124, 1810
Terlevich A. I., Forbes D. A., 2002, MNRAS, 330, 547
Thomas D., Maraston C., Schawinski K., Sarzi M., Silk J., 2010, MNRAS, 404, 1775
Toomre A., 1964, ApJ, 139, 1217
Toomre A., 1977, in Tinsley B. M., Larson D. Campbell R. B. G., eds, Evolution of Galaxies and Stellar Populations. Yale Univ. Press, New Haven, p. 401
Toomre A., Toomre J., 1972, ApJ, 178, 623
Trager S. C., Somerville R. S., 2009, MNRAS, 395, 608
Treu T., Ellis R. S., Liao T. X., van Dokkum P. G., 2005a, ApJ, 622, L5
Treu T. et al., 2005b, ApJ, 633, 174
Trujillo I., Ferreras I., de la Rosa I. G., 2011, MNRAS, 415, 3903
Trujillo-Gomez S., Klypin A., Primack J., Romanowsky A. J., 2011, ApJ, 742, 16
van der Wel A., Franx M., van Dokkum P. G., Rix H.-W., 2004, ApJ, 601, L5
van Dokkum P. G., van der Marel R. P., 2007, ApJ, 655, 30
Wechsler R. H., Bullock J. S., Primack J. R., Kravtsov A. V., Dekel A., 2002, ApJ, 568, 52
Woo J., Courteau S., Dekel A., 2008, MNRAS, 390, 1453
Worthey G., Ottaviani D. L., 1997, ApJS, 111, 377
Worthey G., Faber S. M., Gonzalez J. J., Burstein D., 1994, ApJS, 94, 687
Wuyts S., Cox T. J., Hayward C. C., Franx M., Hernquist L., Hopkins P. F., Jonsson P., van Dokkum P. G., 2010, ApJ, 722, 1666
Yates R. M., Henriques B., Thomas P. A., Kauffmann G., Johansson J., White S. D. M., 2013, MNRAS, 435, 3500
York D. G., Adelman J., Anderson J. E., Anderson S. F., Yanny B., Yasuda N., 2000, AJ, 120, 1579

This paper has been typeset from a TEX/LATEX file prepared by the author.